

Finite-Element Analysis of an Antagonistic Bistable Shape Memory Alloy Beam Actuator

Hamid Shahsavari, Xi Chen, Georgino Kaleng Tshikwand, Frank Wendler, and Manfred Kohl*

A finite-element (FE) analysis of the active bistability of an antagonistic shape memory alloy (SMA) beam actuator of TiNiCu is presented. The actuator comprises two coupled SMA beams that are clamped at both ends and coupled in their center by a spacer having different memory shapes being deflected in opposite out-of-plane directions. The actuator is characterized by two equilibrium positions. To determine bistable behavior as a function of geometrical parameters, a force criterion is defined by the coupling force of the beams in austenitic and martensitic states. Bistable behavior is achieved, if the coupling force does not change sign in the entire displacement range. This implies that the austenitic beam dominates the opposing martensitic beam. Thus, selective heating of the SMA beams results in a snap-through motion of the coupled SMA beams. Depending on which of the two beams is in austenitic state, either of the two equilibrium positions is reached without the need for an external force. It is demonstrated that geometrical parameters like initial predeflection and spacer length have a crucial effect on the bistable performance. Bistable regions as well as critical limits characterized by geometry-dependent stability ratios, beyond which the actuator's performance becomes monostable, are identified.

1. Introduction

Shape memory alloys (SMAs) have gained considerable attention due to their unique ability to undergo reversible phase transformations in response to external stimuli, such as temperature and stress,^[1] as well as magnetic fields.^[2] SMA actuators exhibit exceptional mechanical properties including large displacements

and high forces as well as adaptive structural properties. At the macroscale, these features are of special interest, for example, for thermal SMA actuators that make use of the intrinsic temperature sensing capability of the material by inducing phase transformation via the change of external temperature.^[3] In addition, SMA actuators are driven by direct Joule heating or laser irradiation to perform positioning or switching functions on demand in various engineering applications such as robotics, aerospace, optics, and biomedical devices.^[3–7] Interesting applications are at miniature scales, as power consumption is low and heat transfer is fast due to large surface-to-volume ratios.^[8–10] In the rapidly evolving landscape of microelectromechanical systems, the integration of SMA microactuators emerged as a pioneering and transformative technology.^[11–15] Over the past few decades, extensive research efforts have been directed toward the development


and refinement of SMA film- and SMA foil-based actuators, driven by the need for miniaturized, high-performance devices in various applications.^[11,12,16] Various miniature-scale SMA actuators have been developed in emerging fields like bioanalytics, medical, and miniature control, see, for example, refs. [17,18]

Bistable structures, which can maintain two stable configurations without continuous external power supply, have been a subject of considerable interest in different scales due to their unique mechanical behavior and diverse applications. The various approaches to achieve bistability can be grouped into passive spring-like structures requiring an external actuator to switch between stable states and active structures that change between bistable states due to an external stimulus, for example, an electrical, thermal, or magnetic field. Passive bi-/multistable structures have been developed that can switch between two or more stable configurations.^[19–21] For instance, Niu et al.^[21] introduced a novel approach to enhance the response speed and output force of SMA actuators by combining passive spring-based bistable linkages and SMA springs. In contrast, active bistability without the need for an external force is achieved by merging the bistable compliant structure and SMA actuator in a single component.

Multistable antagonistic actuators based on superelastic cables have been developed^[22] and their application has been explored

H. Shahsavari, X. Chen, M. Kohl
Institute of Microstructure Technology (IMT)
Karlsruhe Institute of Technology (KIT)
76021 Karlsruhe, Germany
E-mail: manfred.kohl@kit.edu

G. Kaleng Tshikwand, F. Wendler
Institute of Materials Simulation
Friedrich-Alexander University of Erlangen-Nürnberg
91054 Erlangen, Germany

 The ORCID identification number(s) for the author(s) of this article can be found under <https://doi.org/10.1002/adem.202400969>.

© 2024 The Author(s). Advanced Engineering Materials published by Wiley-VCH GmbH. This is an open access article under the terms of the Creative Commons Attribution License, which permits use, distribution and reproduction in any medium, provided the original work is properly cited.

DOI: 10.1002/adem.202400969

for the control of large scale adaptive facades.^[23] While there is plenty of work on bistable actuators at the macroscale,^[24] bistable or multistable actuation concepts at the microscale are much less explored. In recent years, bistable SMA microactuators have received increasing interest due to their large work output and large potential for miniaturization.^[25–27] SMA bistable structures have shown potential in the development of micromanipulators, microswitches, and microfluidic devices, where their compact size and precise actuation capabilities are advantageous.^[28–30] Recently, self-actuating SMA systems like resonant self-oscillating devices have been developed for energy harvesting of low-grade waste heat using bidirectional^[31] and bistable actuation.^[25] The methods employed in designing and fabricating these devices encompass a range of techniques, including magnetron sputtering, lithography, laser micromachining, and additive manufacturing, enabling the production of complex geometries with high precision.^[16–18,29]

Previous analytical studies on bistable beams consider a sinusoidal function for the beam geometry of the first buckling mode.^[32–37] In this ideal case, symmetrical force and energy characteristics are obtained that are characterized by two stable states and the absence of monostable behavior. Here, we consider prestraining and antagonistic coupling of SMA beams having different memory shapes, which leads to more complex beam geometries as well as nonsymmetrical force and energy characteristics. Due to the complex beam geometries and boundary conditions, finite-element (FE) simulation is appropriate to calculate the force and energy characteristics.

For material modeling of SMAs, a number of constitutive models have been developed. Brinson and Lammering^[38] introduced a nonlinear FE procedure that employs a thermodynamically derived constitutive law to model SMA behavior, showcasing its versatility in simulating pseudoelasticity and the shape memory effect across different temperature, stress, and loading scenarios. Lagoudas et al.^[39] used micromechanical modeling techniques, including self-consistent approximation-based methods, to analyze the thermomechanical behavior of polycrystalline SMAs, with a focus on comparing various models with experimental data and discussing rate-independent phenomenological models. Arghavani et al.^[40] presented a Hencky-based phenomenological finite strain kinematic hardening constitutive model within the framework of irreversible thermodynamics satisfying the second law of thermodynamics. Sedlak et al.^[41] presented a thermomechanical model for polycrystalline NiTi-based SMAs, capable of simulating complex physical phenomena such as transformations between austenite, R-phase, and martensite, along with martensite reorientation, under general thermomechanical loading, aided by a novel dissipation function and material anisotropy considerations. Sielenkämper and Wulfinghoff^[42] presented a finite-strain SMA model with ability to accurately predict the behavior of SMA trimorph layer composites under thermal loading with high transformation strains and applied the model to simulations of their bistable performance.

This work addresses the design and optimization of bistable SMA microactuators based on antagonistically coupled SMA beams using a validated FE model. Their basic functional unit is a single SMA beam that is clamped at both ends and its memory shape is adjusted to show a deflection of the beam center in

out-of-plane direction. The outline of the article is as follows. At first, we present FE analysis of the force–displacement and energy–displacement characteristics of the single SMA beam in martensitic and austenitic states for different design parameters (Section 3). Based on this analysis, we investigate the antagonistic coupling of two such SMA beams with memory shapes in opposite out-of-plane directions, one being in martensitic and one in austenitic state to enable bistability (Section 4). These results are then compared with FE analysis of the coupled antagonistic SMA beam actuator (Section 5), which requires additional initial simulation steps to adjust the coupling of the SMA beams required for bistable actuation. Based on our assessment, we identify a useful range of geometry parameters, in which the antagonistic SMA beam actuator exhibits bistability.

2. Modeling Approach

2.1. Constitutive Model

The 3D coupled thermomechanical material constitutive model used in this work follows the approach of ref. [26] describing both shape memory effect and superelasticity of SMA materials. This model is suitable to treat the time-dependent behavior of polycrystalline thin SMA film microactuators under large rotations. In particular, it captures the electrothermomechanical coupling upon Joule heating being relevant to SMA actuation problems. Compared to most phenomenological SMA material modeling approaches, the SMA material model employed here considers strain (instead of stress) and temperature as the control variables. The Clausius–Duhem inequality satisfying the second law of thermodynamics^[43] states that in an irreversible process the dissipation d is positive.

$$d = \rho T \dot{s} + \sigma \dot{\epsilon} - \rho \dot{u} - q \cdot \frac{\nabla T}{T} \geq 0 \quad (1)$$

where ρ , T , s , σ , ϵ , u , q are material density, temperature, entropy, total stress, total strain, specific internal energy, and the heat flux, respectively. The Helmholtz Free energy ψ is defined as

$$\begin{aligned} \psi &= \psi(\epsilon, T, \epsilon^{tr}, \xi) = u - sT \\ &= \frac{1}{2\rho} \epsilon : E : \epsilon - \frac{1}{\rho} \epsilon : E : \epsilon^{tr} + c \left[(T - T_0) - T \ln \left(\frac{T}{T_0} \right) \right] - s_0 T + u_0 \end{aligned} \quad (2)$$

From the Coleman–Noll procedure,^[44] we obtain the following constitutive equations

$$\begin{aligned} \sigma &= \rho \frac{\partial \psi}{\partial \epsilon} = E : (\epsilon - \epsilon^{tr}) \\ s &= - \frac{\partial \psi}{\partial T} = c \ln \left(\frac{T}{T_0} \right) + s_0 \\ \phi &= - \rho \frac{\partial \psi}{\partial \epsilon^{tr}} = E : \epsilon \\ \pi &= - \rho \frac{\partial \psi}{\partial \xi} = - \frac{1}{2} \epsilon : \Delta E : \epsilon + \frac{1}{2} \epsilon : \Delta E : \epsilon^{tr} \\ &\quad - \rho \Delta c \left[(T - T_0) - T \ln \left(\frac{T}{T_0} \right) \right] + \rho \Delta s_0 T - \rho \Delta u_0 \end{aligned} \quad (3)$$

where ε^{tr} , ξ , E , c , T_0 , s_0 , u_0 are transformation strain, martensite volume fraction, effective stiffness tensor, the effective specific heat, reference temperature, the effective specific entropy at the reference state, and the effective specific internal energy at the reference state, respectively. Also, ϕ and π are the thermodynamic driving forces conjugate to the internal state variables, ε^{tr} and ξ , respectively. All effective parameters are calculated using the mixture rules combining the corresponding austenite and martensite properties. In this model, we do not consider heat convection because the primary focus is on understanding the bistability of antagonistic SMA beams and investigating the effect of geometrical parameters to determine bistable and monostable regions. Further details of the material model are provided in ref. [26]. The mentioned constitutive model is implemented as a user-defined material subroutine (UMAT) and used in the FEM code ABAQUS.

2.2. Simulation Parameters

The base material of the investigated SMA beam actuators is a $Ti_{53.9}Ni_{30.4}Cu_{15.7}$ film fabricated by magnetron sputtering. Table 1 summarizes the material parameters used here for performance simulations, which have been determined by tensile experiments and differential scanning calorimetry.^[45] Figure 1 shows tensile loading and unloading plots until 2.5% strain at low (296 K) and high (343 K) temperatures corresponding to martensite and austenite conditions, respectively. We obtain good agreement between experimental and FE simulation results in both conditions showing the capability of using the constitutive model to capture the material behavior.

3. Single SMA Beam

At first, we discuss the layout and performance of a single SMA beam, which is the basic functional unit of the antagonistic SMA beam actuator. The single SMA beam is clamped at both ends and its memory shape is adjusted to show a deflection in out-of-plane direction as shown in Figure 2. The SMA beam is clamped at both ends and the beam center of length S is deflected by the distance h in out-of-plane direction. This initial condition can be achieved using a loading element of length S and width w for beam deflection and subsequent heat treatment in deflected

Table 1. Calibrated SMA material parameters used for FEM simulations.

Description	Symbol	Value	Unit
Critical start and finish stresses	$\sigma_{scr}, \sigma_{for}$	40 105	MPa
Maximum transformation strain	ε_{tr}^{max}	0.012	–
Austenite and martensite Poisson ratio	ν_A, ν_M	0.33, 0.33	–
Density	ρ	6450	$kg\ m^{-3}$
Austenite start and finish temperatures	A_s, A_f	333, 343	K
Martensite finish and start temperatures	M_f, M_s	305, 315	K
Clausius Clapeyron coefficients	C_{AM}, C_{MA}	5, 5	$MPa\ K^{-1}$
Austenite and martensite elastic modulus	E_A, E_M	20.3, 15.2	GPa
Heat capacity	c	434	$J(kg\ K^{-1})$

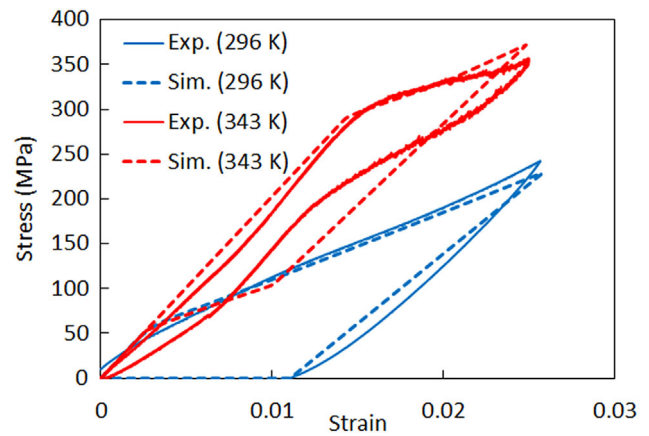


Figure 1. Experimental (Exp.) and simulated (Sim.) stress–strain results of the investigated Ti–Ni–Cu film at 296 K (martensite) and 343 K (austenite). Experimental data are adapted from.^[45]

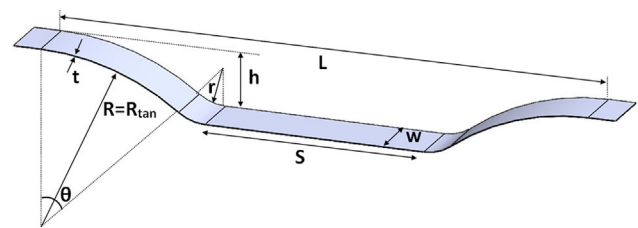


Figure 2. Schematic layout of a single SMA beam that is clamped at both ends and deflected out of plane in the beam center in a loading area of length S . Legend: L , beam length; w , beam width; t , beam thickness; r , bending radius of the beam center; R , bending radius of the beam end; h , initial beam deflection.

condition to memorize the corresponding shape.^[45] Thereby, the length S and the deflection h as well as the bending radius of the curved sections in the beam center r and at the beam ends R are considered as adjustable geometrical parameters. At low bending radius R , a straight section appears between the two curved sections. As the bending radius R increases, the length of this straight section decreases until it becomes zero in the tangential limit of R_{tan} . In this investigation, we consider seven geometrical parameters as illustrated in Figure 2. R_{tan} is a function of the four parameters S , h , L , r as will be discussed in Section 6. The corresponding numerical values are summarized in Table 2. In the following, we investigate the effect of the geometrical parameters on the force–displacement characteristics of the single SMA beam in out-of-plane direction.

Figure 3a illustrates the geometry of a single SMA beam with a displacement applied across its middle section (length S). To determine the total force resulting from this applied displacement, the forces acting on each node within the clamping areas in both sides are summed up. Additionally, the total energy of the single beam is calculated using ABAQUS. Figure 3b shows the effect of bending radius R on the force–displacement characteristics of the single SMA beam in austenitic condition. Loading is applied in displacement control mode at a loading area of length and width S and w , respectively. When increasing the

Table 2. Geometrical parameters used for FEM simulations.

Description	Symbol	Value	Unit
Width of SMA beam	w	1	Mm
Thickness of SMA beam	T	50	μm
Total length of SMA beam	L	10	Mm
Initial deflection of SMA beam	H	0.5, 1, 1.5	mm
Length of loading area	S	3,4,5,6	mm
Bending radius of the beam center	R	0.8	mm
Bending radius of the beam end in tangential limit	$R = R_{\text{tan}}$	Function of (S, h, L, r)	mm

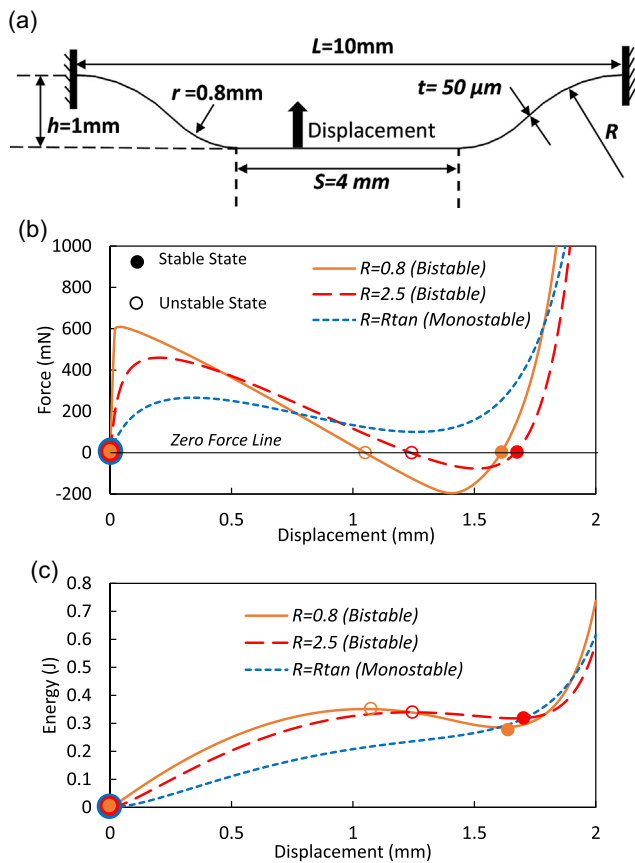


Figure 3. Single SMA beam with memory shape at zero displacement in austenite state at 343 K: a) Schematic of beam geometry and loading direction, b) force versus displacement, and c) energy versus displacement diagrams for different values of bending radius R as indicated.

displacement from the initial memorized state at zero displacement (first stable position), the force shows an initial strong increase followed by a decrease. At low bending radius R , the force decreases to zero by increasing displacement and eventually changes its sign. Upon further increase of displacement, the force reaches a minimum and increases again until it becomes zero and reverses sign again. This performance is a signature of bistability, whereby the deflection reaches an unstable position at

the second zero crossing of the force and then reaches a second stable position at the third zero crossing. At large bending radius in the tangential limit R_{tan} , the zero crossings of the force are absent indicating that the behavior of the SMA beam changes from bistable to monostable. Figure 3c shows the corresponding energy–displacement characteristics of the single SMA beam in austenitic condition. At low bending radius R , two energy minima occur corresponding to two stable equilibrium positions. At large bending radius, the second minimum disappears confirming the transition to monostable behavior.

Figure 4 shows the effect of length S on the force–displacement and energy–displacement characteristics of a single SMA beam in austenitic and martensitic state at room temperature for the case of large bending radius in the tangential limit R_{tan} . In austenitic state, all forces and corresponding energies show monostable behavior as the zero crossings of the force are absent and no second energy minimum occurs, similar to the results presented in Figure 3 (blue dashed lines). By increasing S , both forces and energies are increasing, while maximum and minimum forces are shifting to larger displacements. Also, in martensitic state, all forces and corresponding energies show monostable behavior, similar to the results in austenitic state. By increasing S , forces and energies are increasing, while maximum and minimum forces are shifting to larger displacements. Due to shape memory strain induced in the material in martensitic state and corresponding lower stress values compared to the austenite state, all energy and force values of martensite beams are less than those of austenite ones. In particular, the maximum and minimum forces occur at smaller displacements compared to those in austenitic state.

Figure 5 shows the effect of initial out-of-plane deflection h on the force–displacement and energy–displacement characteristics of single SMA beams in the tangential limit R_{tan} . In austenitic and martensitic state, all forces and corresponding energies show monostable behavior similar to the results presented in Figure 4. As the total displacement course doubles with respect to h , the endpoints rise with increasing values of h . In addition, as h increases, both energy and force values show a rise, and the maximum and minimum forces shift to larger displacements.

4. Antagonistic Coupling of SMA Beams

In the following, we use the results on forces and energies of a single SMA beam to investigate the antagonistic coupling of a martensitic and an austenitic SMA beam. We define the coupling force F^C by the force difference of the two SMA beams ($F^{C1} = -F^{A1} + F^{M2}$ and $F^{C2} = F^{A2} - F^{M1}$), which they exert on each other via an intermediate spacer of dimensions $S \times w \times d$. Since the force direction of the martensite beam is opposite to the austenite one, the coupling force is given by the difference of the respective forces. If F^{C1} is negative for the entire range of displacements of the two SMA beams, the coupled beams are dominated by the shape recovery force $-F^{A1}$ of SMA beam 1 in all cases, that is, they have only one equilibrium position, at which F^{C1} becomes zero. On the other hand, if F^{C2} is positive for the entire range of displacements of the two SMA beams, the shape recovery force F^{A2} of SMA beam 2 dominates in all cases and the coupled beams adopt a second equilibrium position, at

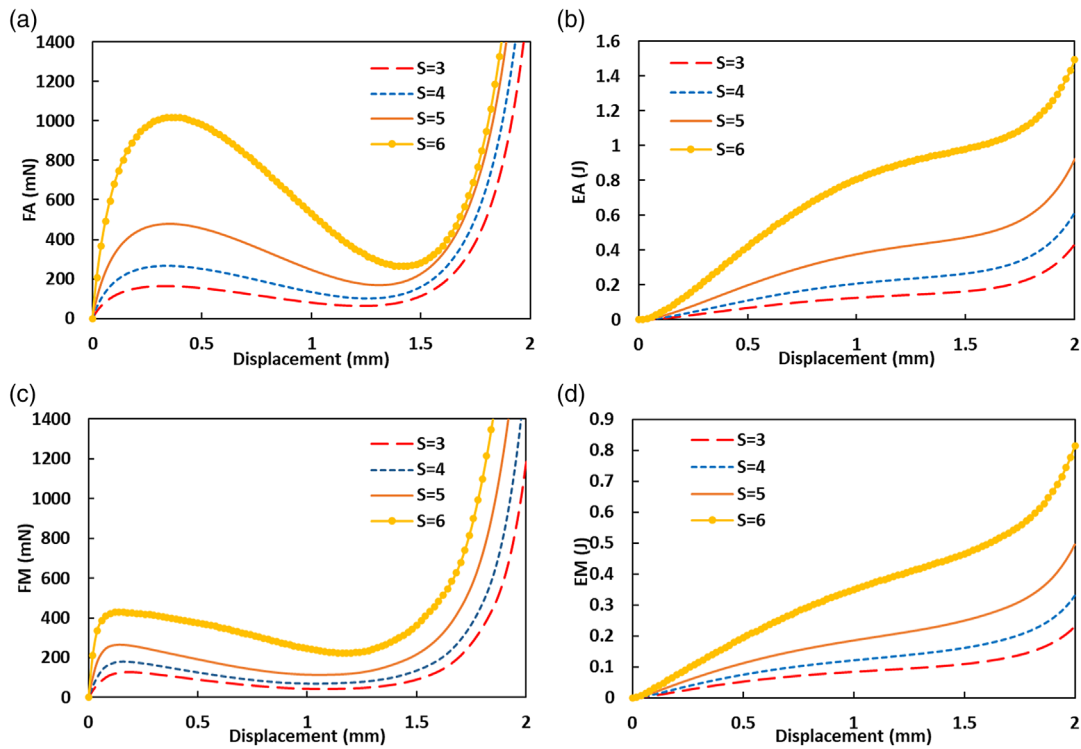


Figure 4. Single SMA beam with memory shape at zero displacement in austenite state at 343 K: a) Force versus displacement, b) energy versus displacement; single SMA beam with memory shape at zero displacement in martensite state: c) force versus displacement, d) energy versus displacement for different lengths S as indicated at initial out-of-plane deflection $h = 1$ mm and bending radius $R = R_{tan}$.

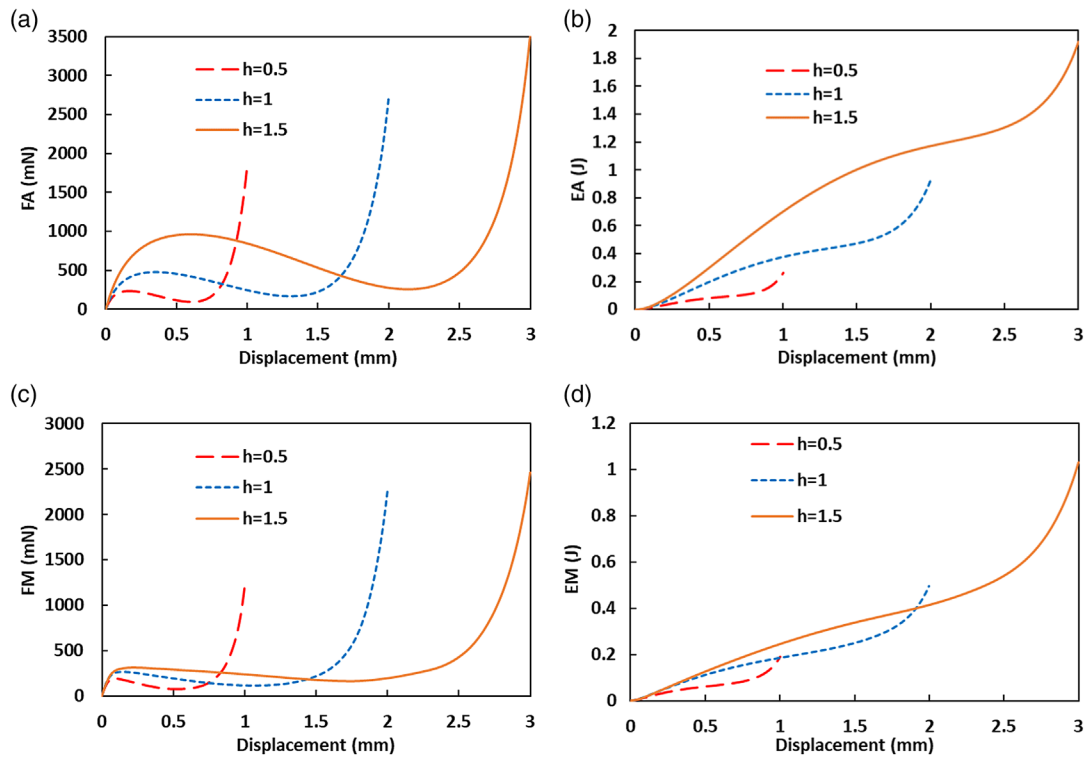


Figure 5. Single SMA beam with memory shape at zero displacement in austenite state: a) force versus displacement, b) energy versus displacement; single SMA beam with memory shape at zero displacement in martensite state: c) Force versus displacement, d) energy versus displacement for different initial out-of-plane deflections h as indicated at length $S = 5$ mm and bending radius $R = R_{tan}$.

which F^{C2} becomes zero. Consequently, we expect bistable behavior of the antagonistically coupled SMA beams, as they can adopt two possible equilibrium positions given by their respective memory shapes. Similarly, we define the coupling energy of the two SMA beams as $E^{Ci} = E^{Ai} + E^{Mj}$ ($i \neq j$). As energy does not depend on direction, we add both energies to calculate the coupling energy. Since the coupling force F^{Ci} is given by the derivative of the coupling energy E^{Ci} , we expect a minimum at the equilibrium position where F^{Ci} becomes zero.

Based on these criteria of coupling force and energy, we investigate the bistability of the antagonistically coupled SMA beams due to a change of phase states using the known characteristics of single SMA beams in austenitic and martensitic states. Thereby, we consider the memory shapes of SMA beams 1 and 2 to be at zero displacement and maximum displacement Δz_{max} , respectively. **Figure 6** illustrates the geometries of the coupled SMA beams. Two cases can be distinguished.

Case 1: In initial condition, SMA beam 1 is austenitic and in fully deflected state Δz_{max} of 2 mm, while SMA beam 2 is martensitic and in undeflected state. Then, the SMA beam system is characterized by the coupling force $F^{C1}(z) = -F^{A1}(z) + F^{M2}(\Delta z_{max} - z)$, which drives the system from the position $z = \Delta z_{max}$ in negative direction toward the equilibrium position near the memory shape at $z = 0$. Similarly, the coupling energy is determined by $E^{C1}(z) = E^{A1}(z) + E^{M2}(\Delta z_{max} - z)$.

Case 2: In initial condition, SMA beam 2 is austenitic and in fully deflected state at $z = 0$, while SMA beam 1 is martensitic and in undeflected state. Then, the SMA beam system is characterized by the coupling force $F^{C2}(z) = F^{A2}(\Delta z_{max} - z) - F^{M1}(z)$, which drives the system from the position $z = 0$ in positive direction toward the equilibrium position near the memory shape of beam 2 at $z = \Delta z_{max}$. Similarly, the coupling energy is determined by $E^{C2}(z) = E^{A2}(\Delta z_{max} - z) + E^{M1}(z)$.

Figure 7a,b show coupling force and energy versus displacement characteristics at different spacer lengths S for case

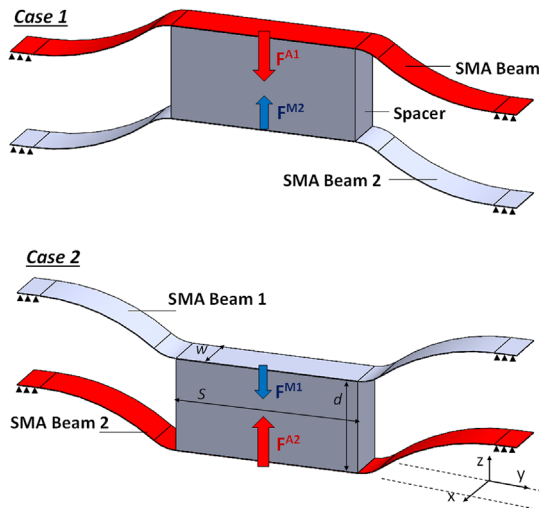


Figure 6. Schematic of the antagonistic coupling of a martensitic and an austenitic SMA beam which are fixed at both ends. Coupling is achieved via an intermediate spacer of dimensions $(S \times w \times d)$. The antagonistic coupling results in two possible equilibrium positions (cases 1 and 2) given by the memory shapes of the SMA beams.

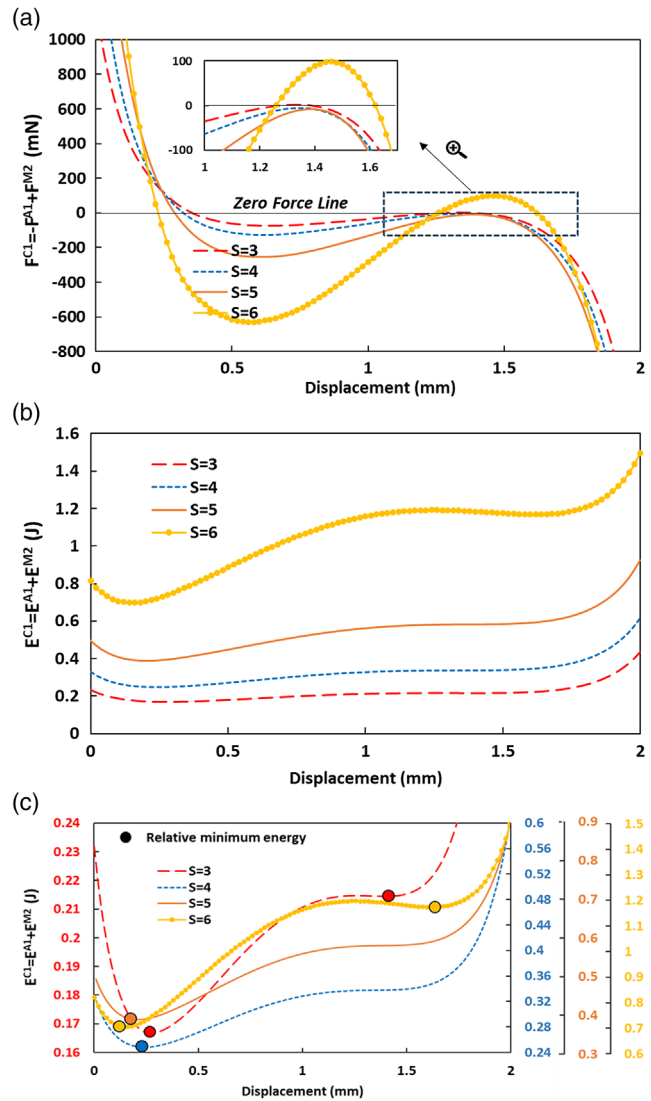


Figure 7. a) Coupling force versus displacement $F^{C1}(z) = -F^{A1}(z) + F^{M2}(\Delta z_{max} - z)$, b) coupling energy versus displacement $E^{C1}(z) = E^{A1}(z) + E^{M2}(\Delta z_{max} - z)$, and c) zoom plot of energy versus displacement with highlighted relative minimum energies in case 1 (illustrated in Figure 6) for different spacer lengths S as indicated at $h = 1$ mm and $R = R_{tan}$.

1, in which SMA beam 1 is in austenitic state starting from fully deflected state Δz_{max} , while SMA beam 2 is in martensitic state starting from undeflected state. In the initial fully deflected state Δz_{max} , the large coupling force F^{C1} drives the system toward equilibrium position 2 near $z = 0$ (case 2). At intermediate spacer lengths S of 4 and 5 mm, F^{C1} stays negative in the full displacement range allowing the coupled system to reach equilibrium position 2, at which F^{C1} becomes zero. However, for S of 3 and 6 mm, the minimum coupling force F^{C1}_{min} decreases and eventually becomes zero. Therefore, the coupling force F^{C1} becomes zero already at an intermediate position, at which the system is expected to stop moving.

Based on these results, we come to the following conclusions. 1) The bistable performance of the coupled SMA beam system due to a change of phase states is only achieved for intermediate spacer lengths between 4 and 5 mm following the criterium of coupling force F^{C1} (case 1). 2) Other antagonistically coupled SMA beam systems with spacer length $S < 3$ and $S > 5$ mm are monostable and do not switch back when changing the phase states. 3) Similar curves compared to Figure 7a can be constructed for case 2, showing mirror symmetry in force and displacement. Thus, similar S dependencies are obtained based on the criterium of coupling force F^{C2} (case 2), which are presented in Figure B1 in Appendix B. The numerical values of maximum and minimum are summarized in Table A1 in Appendix A.

The corresponding energy–displacement characteristics (Figure 7b) show that by increasing S , the total energy of the system is increased. Due to different scales of energy for $S = 3$ to 6 mm, we magnify each energy plot based on corresponding colored Y axes in Figure 7c to better investigate the energy of the system. This figure shows one energy minimum at intermediate spacer lengths S of 4 and 5 mm. This is expected, as the force in a system is proportional to the first derivative of energy. Once the force becomes zero and the force change is positive, the system adopts a stable state with a relative energy minimum. As the antagonistically coupled SMA beam system shows bistable performance when the coupling force becomes zero at only one position (equilibrium position), the corresponding coupling energy will exhibit only one relative minimum, one for each case 1 and 2. Figure 7c shows that the coupling energy exhibits two relative minima for spacer lengths $S = 3$ mm and $S = 5$ mm. In these cases, the bistability of single SMA beams gives rise to monostable behavior of corresponding antagonistically coupled SMA beam systems.

Figures 8a,b show coupling force and energy versus displacement characteristics at different beam deflections h for case 1. The coupling force F^{C1} drives the system toward equilibrium position 2 near $z = 0$ starting from the fully deflected state at Δz_{\max} . At beam deflections h of 1 and 1.5 mm, F^{C1} stays negative in the full displacement range and, thus, the coupled system reaches equilibrium position 2, at which F^{C1} becomes zero. Therefore, we conclude that bistable performance of the coupled SMA beam system is achieved for beam deflections h of 1 and 1.5 mm according to the force criterium of coupling forces (case 1). At smaller deflection h of 0.5 mm, the minimum coupling force F_{\min}^{C1} becomes zero at an intermediate position. Therefore, coupled SMA beam systems with small deflection h of 0.5 mm are monostable. Similar to previous study on spacer length S , Figure 8b shows that by increasing h , the total energy of the system is increased. Due to different scales of energies in Figure 8b, we magnify each energy plot based on corresponding colored Y axes in Figure 8c to better investigate the energy of the system. In addition, we use dimensionless displacements divided by h , since the displacement courses of systems are different. This figure shows one energy minimum for beam deflections h of 1 and 1.5 mm and two energy minima for h of 0.5 mm, which agrees with force–displacement diagram. Similar performance occurs for case 2, which is presented in Figure B2 in Appendix B. The numerical values of maximum and minimum forces are summarized in Table A2 in Appendix A.

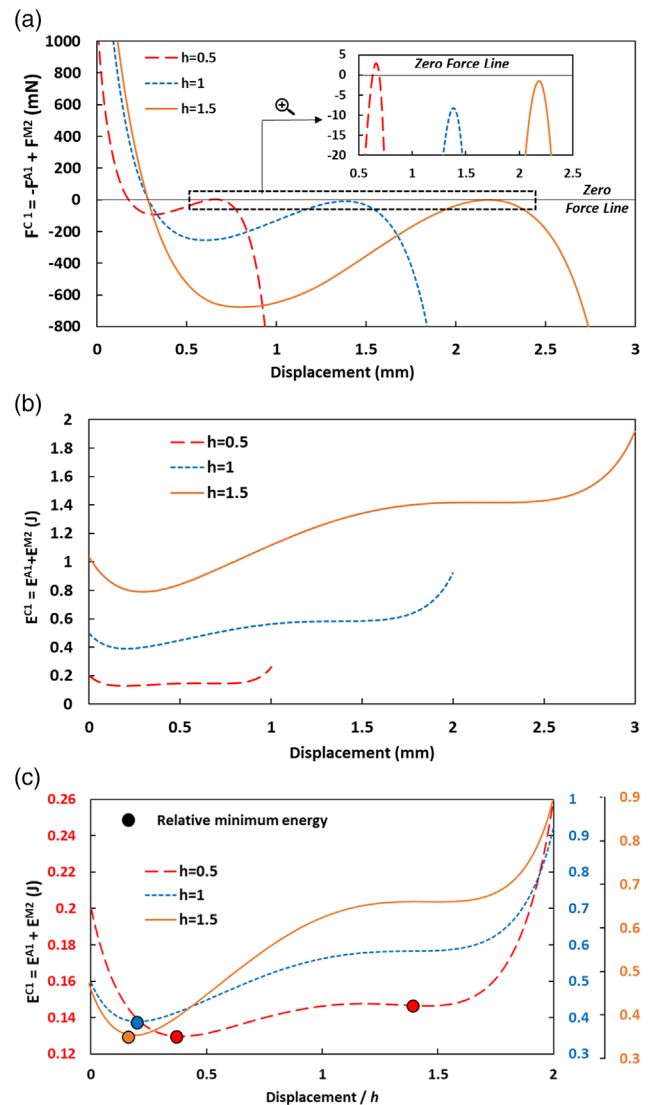


Figure 8. a) Coupling force versus displacement $F^{C1}(z) = -F^{A1}(z) + F^{M2}(\Delta z_{\max} - z)$, b) coupling energy versus displacement $E^{C1}(z) = E^{A1}(z) + E^{M2}(\Delta z_{\max} - z)$, and c) zoom plot of energy versus dimensionless displacement with highlighted relative minimum energies in case 1 (illustrated in Figure 6) for different beam deflections h as indicated at $S = 5$ mm and $R = R_{\tan}$.

5. Antagonistic SMA Beam Actuator

5.1. Layout and Operation Principle

Figure 9 shows a schematic of the antagonistic SMA beam actuator and the simulation procedure to adjust the initial condition for bistable actuation. The beam actuator consists of two SMA beams each having a memory shape being deflected in opposite out-of-plane directions. The SMA beams are coupled in their center by a spacer of length S , width w , and height d . The SMA beam ends are attached to two base parts of a thermally insulating polymer. Further components are two heat sources placed at the top and bottom side of the coupled SMA beams. Among the different

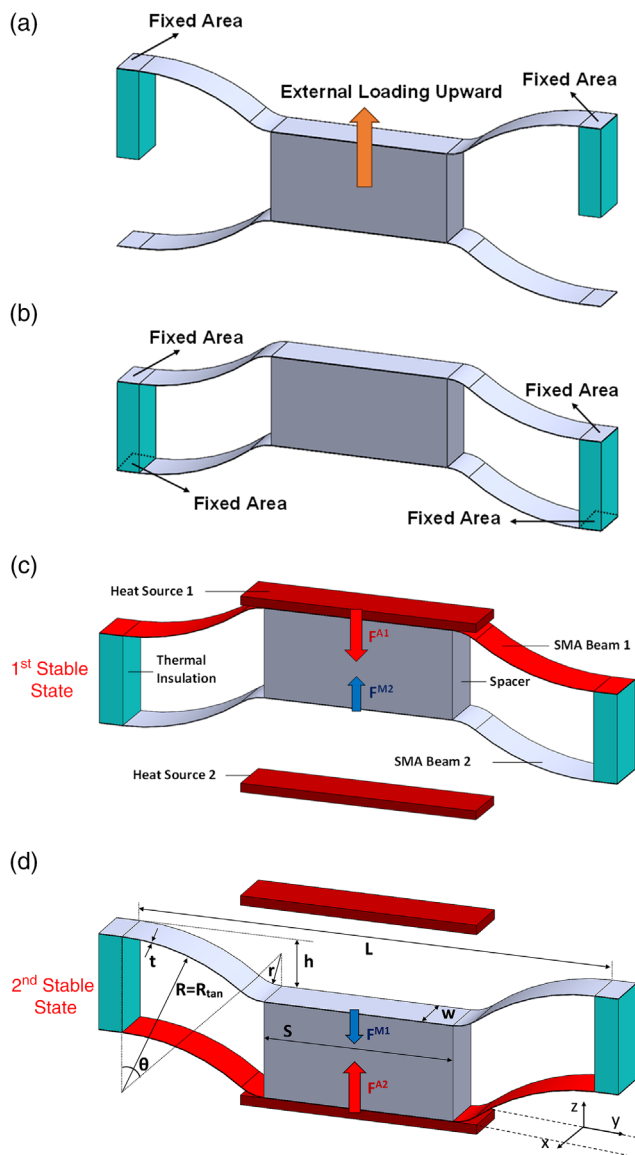


Figure 9. Schematic layout of the antagonistic SMA beam actuator and the simulation procedure to adjust the initial condition for bistable actuation. a) step 1: Applying an external load in upward direction on the fixed SMA beam 1, while SMA beam 2 is unconstrained. Both beams are in their stress-free memory shape; b) step 2: fixing both ends of SMA beam 2 and removing the load; c) step 3: heat transfer from heat source 1 to SMA beam 1 causing a shape recovery force to push the coupled beams to the second stable state; d) step 4: heat transfer from heat source 2 to SMA beam 2 with heat source 2 causing a shape recovery force to push the coupled beams to the first stable state.

geometrical parameters, the spacer length S and beam deflection h are of special interest as the results of our simulations of single beams indicate. Thereby, we keep the length L , width w , and thickness t of the SMA beams constant using typical values that are accessible in the experiment. Following the results on single SMA beams, the bending radius r is set to 0.8 mm. In this case, the bending radius in the tangential limit R_{tan} can be expressed as a function of the other geometrical parameters using Equation (C1) given in the Appendix C.

Generally, there are three options to model the predeflected memory shapes of the antagonistic SMA beam actuator: (1) applying an axial compressive force on a straight SMA beam until it deflects to the shape of the first mode of buckling and then fixing two both beam ends; (2) starting from a predeflected beam which is geometrically similar to the buckled shape and fixing both beam ends; and (3) combining (1) and (2) by applying an axial compressive force on a predeflected SMA beam to adjust the out-of-plane deflection before fixing both beam ends. Here, we use option (2), that is, we consider stress-free predeflected SMA beams with their buckled shapes being their memory shapes. In experiment, the memory shapes can be adjusted by heat treatment of the SMA beams in constraint condition.^[45]

In the following, we consider two predeflected SMA beams with maximum deflections of $\pm h$ in out-of-plane directions, which are connected in their center by a spacer. A tie constraint is established between the contact areas of the beams and the spacer. Additionally, we employ quadratic sweep hexagonal elements with reduced integration from the coupled temperature-displacement element (C3D20RT) (A 20-node thermally coupled brick, triquadratic displacement, trilinear temperature, reduced integration) family to mesh all components. The analysis of the fully coupled antagonistic SMA beam actuators requires four transient loading steps as follows:

Step 1, Figure 9a: Both ends of the top beam (SMA beam 1) are clamped and a linear displacement of $2h$ is applied at the center of the assembly in upward (z -) direction. In this step, the spacer is attached to both beams and due to its displacement, it rigidly pulls the bottom beam (SMA beam 2) upward. Thereby, the temperature of both SMA beams is at room temperature (296 K). Thus, significant stress occurs in some parts of the top SMA beam as it departs from its memory shape. This causes a transition of initially twinned martensite to partial or total detwinned martensite.

Step 2, Figure 9b: Both ends of the bottom SMA beam, which is still in its memory shape, are clamped and the load of step 1 is removed. Thereby, the elastic part of the total strain is released, while the quasiplastic part (shape memory strain) in the top SMA beam still remains. Thus, the top SMA beam relaxes back downwards to some extent and consequently pushes the bottom SMA beam downward as well. The resulting state of the coupled beam system is the first equilibrium position (first stable state) of the antagonistic SMA beam actuator.

Step 3, Figure 9c: Once the first stable state is established, two heat sources are placed at the top and bottom sides of the SMA beams to enable selective heat transfer via separate solid–solid contacts. Once SMA beam 1 touches the top heat source, its temperature increases until it transforms to austenite (at $T > A_s$), while SMA beam 2 stays in martensitic condition. The resulting shape recovery force F^{A1} caused by the shape memory strain in step 1 pushes SMA beam 2 downward and generates an opposing force F^{M2} . At sufficiently large shape recovery force $F^{A1} > F^{M2}$, a dynamic jumping motion occurs driving the coupled system in negative direction downward to its second stable equilibrium position (second stable state).

Step 4, Figure 9d: SMA beam 2 is fully deflected and touches the bottom heat source, while SMA beam 1 reaches its undeformed memory state and cools down again. Subsequent heating of SMA beam 2 generates the shape recovery

force F^{A2} and pushes SMA beam 1 upward. A dynamic jumping motion occurs in opposite direction toward the first equilibrium position once a sufficiently large shape recovery force $F^{A2} > F^{M1}$ is reached.

Thus, repeated selective heating of the SMA beams (in steps 3 and 4) causes periodic self-actuation of the coupled system resulting in an oscillatory bistable motion between the two equilibrium positions. This simplified approach suggests that the coupling force $F^{C1}(z) = -F^{A1}(z) + F^{M2}(\Delta z_{\max} - z)$ is negative and $F^{C2}(z) = F^{A2}(\Delta z_{\max} - z) - F^{M1}(z)$ is positive to obtain bistable behavior of the coupled antagonistic SMA beams.

5.2. Performance of Antagonistic Actuation

Figure 10 shows the force–displacement and energy–displacement characteristics of an antagonistic SMA beam actuator with spacer length S of 4 mm and predeflection h of 1 mm during adjustment of the initial condition for bistable actuation and during bistable actuation as illustrated in Figure 9a,b and Figure 9c,d, respectively. In this case, we expect bistable switching from our analysis of the coupling of two antagonistic SMA beams presented in Section 4. During the first step (Figure 10a, blue line), SMA beam 1 moves upward in positive z -direction. The force–deflection characteristic shows the typical performance of a single SMA beam in martensitic state (compare Figure 4a) as SMA beam 2 does not exert any force on SMA beam

1 during this step. During step 2 (green line), SMA beams 1 and 2 are coupled. They move downward to their first equilibrium position (stable state 1) during force relaxation and the net force of both beams decreases to zero. After step 2, the initial condition for bistable actuation is reached.

The subsequent steps 3 and 4 describe the bistable actuation in downward (red line) and upward direction (yellow line), respectively. Downward motion is induced by selective heating of SMA beam 1, while in contact to heat source 1. During heating, the shape recovery force F^{A1} first increases and pushes the coupled system backward, while the opposing force of SMA beam 2 in martensitic state F^{M2} increases as well. The resulting net force F^{C1} shows an initial decrease followed by an intermediate force maximum. However, F^{C1} remains negative in the entire displacement range, as the shape recovery force $-F^{A1}$ dominates F^{M2} . Therefore, the coupled SMA beam system jumps downward to the second stable state. Similarly, upward motion is induced by selective heating of SMA beam 2 while in contact to heat source 2. In this case, the resulting shape recovery force F^{A2} exceeds the opposing force of SMA beam 1 in martensitic state F^{M1} , and the resulting net force F^{C2} stays positive in the entire displacement range. Consequently, the coupled system jumps upward back to the first stable state, where the process of step 3 and 4 repeats causing a self-actuated oscillatory motion.

Figure 10b shows the corresponding energy–displacement characteristics during the four loading steps. During step 1, external energy is applied causing the large energy increase, which decreases slightly in step 2 due to relaxation of the coupled beam system until the local energy minimum in stable state 2 is reached. Steps 3 and 4 reveal the switching between stable states by crossing the energy barrier in between. The energy minimum of stable state 1 is higher than of 2 due to an asymmetry between the two states caused by the initial loading conditions applied here for bistable actuation. This becomes obvious when investigating the corresponding contour plots of deflection and von Mises stress of the antagonistic SMA beam actuator shown in **Figure 11**. The graph highlights that the maximum von Mises stress of the SMA beams in stable states 1 and 2 represented by the red color occurs near the fixed ends of the SMA beams and in proximity to the spacer. These sections experience the maximum shape change during phase transformation. Notably, the intermediate regions between the fixed ends and the spacer exhibit the lowest stress as shown in blue color. The different stress levels and distributions shown in Figure 11a,b confirm the difference of energy levels of the two stable states shown in Figure 10b. Within the beam's width, the stress varies between the edges and the center indicating that the fully 3D simulation shown here is indeed justified without any assumptions such as 2D plane stress or plane strain constraints in the width direction. The details of FE simulations are presented in Table D1 in Appendix D. In our analysis, the mesh size is iteratively refined to achieve convergence in the results.

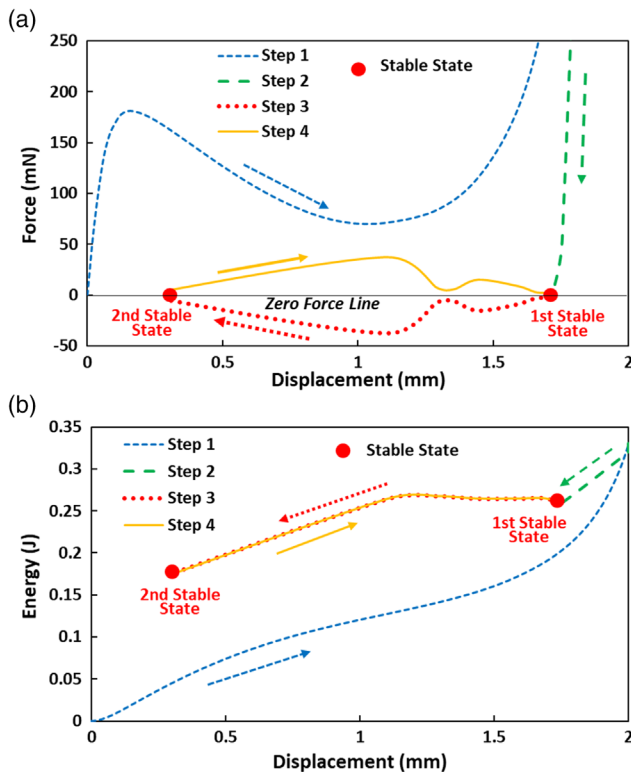


Figure 10. Force and energy diagrams of coupled SMA beams for a geometry of $w = 1$ mm, $t = 50$ μ m, $L = 10$ mm, $h = 1$ mm, $S = 4$ mm, $r = 0.8$ mm, and $R = R_{\text{tan}}$. a) Force versus displacement of coupled SMA beams and b) energy versus displacement of coupled SMA beams for the loading steps 1–4.

6. Discussion

In this study, we conduct a comprehensive FEM simulation to investigate the bistability behavior of antagonistic SMA beam

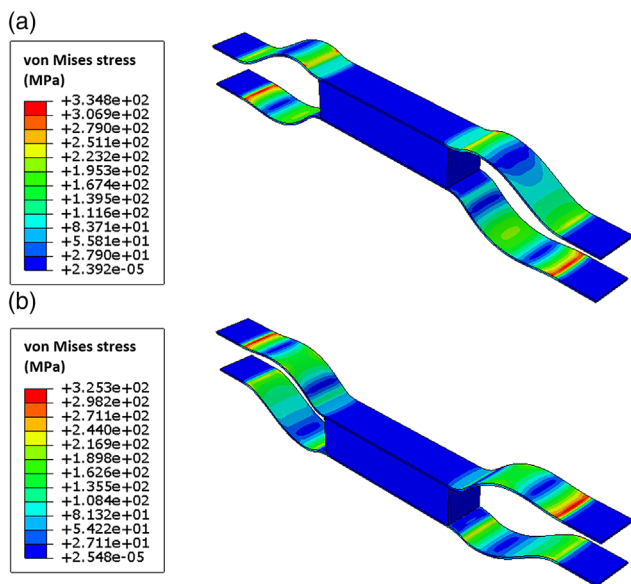


Figure 11. Von Mises stress distribution of the antagonistic SMA beams in stable states 1 and 2 for a geometry of $w = 1$ mm, $t = 50$ μ m, $L = 10$ mm, $h = 1$ mm, $S = 4$ mm, $r = 0.8$ mm, and $R = R_{\text{tan}}$. a) First stable state (SMA beams 1 and 2 are in austenitic and martensitic state, respectively) and b) second stable state (SMA beams 1 and 2 are in martensitic and austenitic state, respectively).

actuators, which consist of two coupled SMA beams with different memory shapes being deflected in opposite out-of-plane directions. The FE model of the SMA material is validated by comparing simulated stress–strain characteristics with experimental results on a $\text{Ti}_{53.9}\text{Ni}_{30.4}\text{Cu}_{15.7}$ film.^[45] Using a coupled thermomechanical SMA constitutive model developed in ABAQUS, first, we perform FE simulations at both austenite and martensite temperatures (shown in Figure 1) and calibrate the model material properties (tabulated in Table 1). Then, a pre-shaped geometry is designed for single SMA beam (Figure 2) with specific geometrical parameters shown in Table 2. Through conducting FE simulations to explore the effect of the bending radius R on the force–displacement characteristics of a single SMA beam in the austenitic state, it is observed that zero force crossings do not occur at the maximum bending radius within the tangential limit, denoted as R_{tan} (Figure 3). This implies a transition in the behavior of the single SMA beam from bistable to monostable, which is an essential requirement for a bistable coupled antagonistic SMA beam actuator. Therefore, we fix the bending radius R to R_{tan} in the subsequent simulations. Our subsequent investigation is performed in three steps.

We characterize the force–displacement and energy–displacement characteristics of single SMA beams with out-of-plane memory shapes in martensitic and austenitic state. A parametric study is conducted on spacer length S and initial deflection of SMA beam h . We show that forces and corresponding energies show monostable behavior in all cases. Both, forces and energy values are increased by increasing S and h , while maximum and minimum forces are shifting to larger

displacements. Numerical values on minimum and maximum forces are presented in Table A1 and A2.

The antagonistic coupling of two such SMA beams via an intermediate spacer is investigated, one being in martensitic and one in austenitic SMA state, causing two opposing forces. The coupling force F^{Ci} , which the SMA beams exert on each other, is given by the force difference of the two SMA beams. We present the characteristics of coupling force and corresponding energy for different spacer lengths S and initial deflections of SMA beam h and analyze their effect on bistability. We find that the antagonistic coupling of the SMA beams results in a bistable behavior when changing the phase states of the SMA beams, if F^{Ci} does not change sign in the entire displacement range. This implies that the austenitic beam dominates the performance of the opposing martensitic beam at all displacements. Thus, selective heating of the SMA beams results in a snap-through motion of the coupled beam system between their equilibrium positions without the need for an external force. For the investigated design parameters, active bistable performance is achieved for intermediate spacer lengths S between 3 and 6 mm.

We characterize the force–displacement and energy–displacement characteristics of antagonistic SMA beam actuators. Unlike the analysis of single SMA beams in austenite or martensite state and of their coupled performance in one loading step, the analysis of the fully coupled antagonistic SMA beam actuators requires two initial simulation steps to adjust the coupling of the SMA beams. We exemplarily show the performance of force and energy of an antagonistic SMA beam actuator with spacer length S of 4 mm and initial predeflection h of 1 mm. The actuator exhibits two equilibrium positions, which verify the bistability criterion presented in the previous step. The displacement versus force characteristic of the actuator will show a hysteresis when propagating between the equilibrium positions under the condition of force control, which is given by the difference of maximum forces in forward and reverse direction. These positions correspond to two different energy levels of stable states, which can be explained by the different loading conditions that are obtained after the initial loading steps needed to couple the antagonistic SMA beams. The different loading conditions are verified by the different stress distributions in the two stable states of the actuator.

The presented model does not consider heat convection because the primary focus is on understanding the bistability of antagonistic SMA beams and investigating the effect of geometrical parameters. Due to this assumption, the performance of the SMA beam actuators can be predicted for applications at sufficiently low frequency when keeping stable positions over longer times. The cooling time required for transformation back to martensite depends on the thermal mass as well as the cooling mechanism (heat conduction, active/passive heat convection). If switching occurs more rapidly compared to the cooling time, heat will accumulate and cause incomplete phase transformation, resulting in reduced or even no performance.

Our FEM simulations for different geometries of antagonistic SMA beam actuators suggest to distinguish three different stability regions including two monostable regions #1 and #2 and a bistable region #3 as shown in Figure 12. For a given predeflection h , increasing the spacer length S , the peak force of the opposing martensitic SMA beam strongly increases. Thus, the

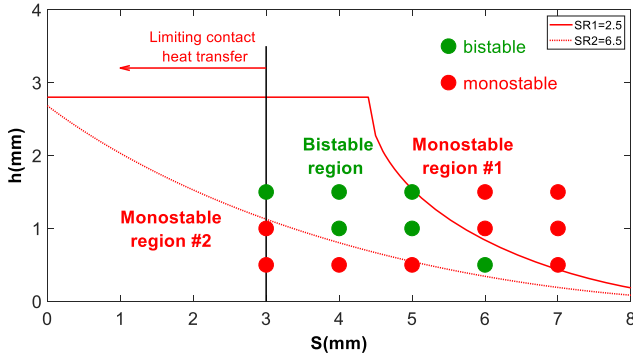


Figure 12. Parameter range of spacer length S and predeflection h defining the regions of bistable and monostable behavior of the antagonistic SMA beam actuators. The limiting functions defining monostable regions #1 and #2 are indicated by red lines.

required force of the austenitic SMA beam must increase as well to maintain bistability, which is no longer fulfilled at large S values. On the other hand, by reducing the spacer length S , the maximum stress of the SMA beam decreases and, thus, the maximum force of the SMA beam being in austenitic state eventually becomes too small. As a result, we find bistable behavior only at intermediate spacer lengths S for a given predeflection h . The bistability region is highlighted in Figure 12 by red and green circles. The bistability region can be characterized by defining the stability ratio SR , which is given by the ratio of R_{tan} and the bending radius of the beam center r ($SR = R_{tan}/r$). Then, the different bistable and monostable regions can be determined by the lower and upper limiting values $SR1$ and $SR2$, respectively.

$$\begin{aligned} \text{(Monostable region1)} \quad & SR1 < \frac{R_{tan}}{r} \text{ (Bistable region)} \\ & < SR2 \text{ (Monostable region2)} \end{aligned} \quad (4)$$

For the investigated antagonistic SMA beam actuators, we find $SR1$ and $SR2$ to be 2.5 and 6.5, respectively. The dependencies of geometrical parameters allow to determine critical values of predeflection h for the different monostable and bistable regions. As described in detail in the Appendix C, we obtain

$$R_{tan} = \frac{(L - S)^2}{8h} + \frac{h}{2} - r \quad (5)$$

$$h = (R_{tan} + r) - \sqrt{(R_{tan} + r)^2 - \left(\frac{L - S}{2}\right)^2} \quad (6)$$

Using the following two equations $SR1 = R1_{tan}/r = 2.5$ and $SR2 = R2_{tan}/r = 6.5$ deduced from (4) and (5), two functions (7) and (8) are obtained for the monostable regions #1 and #2, which are shown in Figure 12 by red lines.

$$h = r \left(SR1 + 1 - \sqrt{(1 + SR1)^2 - \frac{(L - S)^2}{4r^2}} \right) \quad (7)$$

for monostable region 1

Table 3. Switching force (F_{sw}), energy minima (E_{min}), and energy barrier (ΔE_B) of the investigated bistable antagonistic SMA beam actuators for different values of predeflection h and spacer length S (see Figure 12, green dots).

Predeflection [mm]	Spacer length [mm]	Switching force F_{sw} [mN]	Energy minima E_{min} [J]	Energy barrier ΔE_B [J]
$h = 0.5$	$S = 6$	3.76	0.276	0.091
	$S = 5$	8.32	0.387	0.187
$h = 1$	$S = 4$	5.31	0.248	0.087
	$S = 5$	1.57	0.789	0.629
$h = 1.5$	$S = 4$	10.4	0.482	0.253
	$S = 3$	5.98	0.322	0.128

$$h = r \left(SR2 + 1 - \sqrt{(1 + SR2)^2 - \frac{(L - S)^2}{4r^2}} \right) \quad (8)$$

for monostable region 2

It is noteworthy to mention that for small spacer lengths S of 3 mm and below, the maximum force of the SMA beam being in austenitic state eventually becomes too small to enable a good solid–solid contact for heat transfer. This limit is indicated in Figure 12 by an additional line.

By understanding the geometrical constraints and critical factors that govern bistability, we can design and optimize dedicated actuators for switching applications. Typical performance metrics are switching force F_{sw} , energy minimum E_{min} , and energy barrier ΔE_B . Based on our results, the switching force is determined as the minimum value of the coupling force F_{min}^C and the energy minimum as the minimum value of the coupling energy F_{min}^C . Table 3 summarizes these metrics for the geometrical parameters h and S , giving rise to bistability of the antagonistic SMA beam actuator, as displayed in Figure 12 by green dots. In previous work on bistable SMA microactuators, switching forces have been reported in the range of several mN to 120 mN,^[25,30] which is in line with the presented results. Based on our FE simulations, it is possible to tune the performance metrics of the antagonistic SMA beam actuators by adjusting the h and S values. In particular, energy minima increase by increasing S for a given h value and by increasing h for a given S value. Maximal switching forces are obtained in the middle of the bistable region indicated in Figure 12 by the boundary lines of $SR1 = R1_{tan}/r = 2.5$ and $SR2 = R2_{tan}/r = 6.5$. For instance, at $h = 1.5$, the switching force shows a maximum at intermediate spacer length $S = 4$.

7. Conclusion

We present a comprehensive FE simulation study on the active bistability of antagonistic SMA beam actuators using a validated thermomechanical SMA constitutive model. Active bistability means that switching between the two equilibrium positions

is achieved by the actuator itself without the need for an external loading mechanism. The antagonistic SMA beam actuator comprises two monostable SMA beams that are clamped at both ends and coupled in their center by a spacer having memory shapes deflected in opposite out-of-plane directions. The detailed features of the coupled SMA beams give rise to complex asymmetric characteristics of force and energy resulting in mono- or bistable performance depending on the beam geometry. Here, we consider TiNiCu beams of 50 μm thickness and lateral beam dimensions of $10 \times 1 \text{ mm}^2$. The major results are summarized as follows.

1) At first, we present FE analysis of the force–displacement and energy–displacement characteristics of a single SMA beam in martensitic and austenitic states for different design parameters. Thereby, the objective is to identify the parameters giving rise to monostable behavior of a single SMA beam in austenitic state, which is an essential but not sufficient requirement to achieve bistable behavior of antagonistically coupled SMA beams. We find that the zero crossings of the force are absent at the large bending radius in the tangential limit indicating that the behavior of the SMA beam changes from bistable to monostable. This result is in line with the disappearance of the second minimum in energy displacement characteristics confirming the transition to monostable behavior. Furthermore, for all investigated spacer lengths s and initial out-of-plane deflections, the force–displacement and energy–displacement characteristics in austenitic and martensitic states show monostable behavior in the tangential limit.

2) Based on the results on single SMA beams, we determine the performance of two antagonistically coupled SMA beams. For the design of bistable antagonistic SMA beam actuators, the SMA beams are considered to be in opposite phase states, one being in martensitic and one in austenitic state, while the memory shapes of the SMA beams are in opposite out-of-plane directions. We find that the coupling force given by the counteracting forces of the two SMA beams must not change sign in the entire displacement range to obtain bistability. This condition implies that the austenitic beam always dominates the opposing martensitic beam. Thus, selective heating of the SMA beams results in a snap-through motion of the coupled beam system between their equilibrium positions without the need for an external loading mechanism. For the investigated design parameters, such active bistable performance is achieved for intermediate spacer lengths between 4 and 5 mm.

3) Finally, we compare the results on two coupled SMA beams with FE analysis of the coupled antagonistic SMA beam actuator, which requires two additional initial simulation steps to adjust the coupling of the SMA beams required for bistable actuation. Both results are in line allowing to predict the geometry dependencies of bistability. Our detailed FE analysis allows to determine the course of force versus displacement in both forward and backward directions when selectively heating the SMA beams. In addition, the corresponding energy versus displacement characteristics are determined including the energy barrier that needs to be overcome for bistable switching and the point of instability, at which the energy barrier is reached. Depending on the geometry parameters, our analysis allows to identify bistable regions as well as critical limits

characterized by stability ratios, beyond which the actuator's performance becomes monostable.

The development of actuators showing active bistability without the need for external loading is of special interest for miniature-scale switching applications. The simple design of the antagonistic SMA beam actuator comprising two counteracting SMA beams allows for compact solutions featuring large actuation stroke and large switching force. Typical applications are, for instance, positioning tasks or manipulation of small objects. Furthermore, the actuator design has a large potential for further size reduction to the micrometer scale using dedicated SMA microtechnologies.^[12–14] Thus, novel SMA switching devices can be realized, such as bistable micro-optical switches or bistable microvalves. Further extension of bistable to advanced multistable SMA actuators will open up new options in the emerging fields of digital micromechanical systems and digital microfluidics as well as mechanically active metamaterials.

Appendix A

Table A1. Maximum and minimum forces of single SMA beams in austenite (a) and martensite (M) states and coupling force for different lengths of loading area S at fixed initial out-of-plane deflection $h = 1 \text{ mm}$ and bending radius of the SMA beam end in tangential limit $R = R_{\text{tan}}$.

Value	Geometrical Parameters ($h = 1 \text{ mm}$, $R = R_{\text{tan}}$)			
	$S = 3 \text{ mm}$	$S = 4 \text{ mm}$	$S = 5 \text{ mm}$	$S = 6 \text{ mm}$
F_{max}^A (mN)	163.4	266.2	478.6	1018.1
F_{min}^A (mN)	62.7	100.7	168.1	263.4
F_{max}^M (mN)	128.4	181	265.9	429.5
F_{min}^M (mN)	43.1	69.9	114.5	224.1
F_{max}^C (mN)	74.4	128.3	253.6	630.2
F_{min}^C (mN)	−1.4	5.3	8.3	−98.4

Table A2. Maximum and minimum forces of single SMA beams in austenite (a) and martensite (M) states and coupling force for different initial out-of-plane deflections h at fixed lengths of loading area $S = 5 \text{ mm}$ and bending radius of the SMA beam end in tangential limit $R = R_{\text{tan}}$.

Value	Geometrical Parameters ($S = 5 \text{ mm}$, $R = R_{\text{tan}}$)		
	$h = 0.5 \text{ mm}$	$h = 1 \text{ mm}$	$h = 1.5 \text{ mm}$
F_{max}^A (mN)	236.2	478.6	962.8
F_{min}^A (mN)	95.7	168.1	257.6
F_{max}^M (mN)	191.2	265.9	312.1
F_{min}^M (mN)	73.9	114.5	162
F_{max}^C (mN)	93	253.6	677.6
F_{min}^C (mN)	−3	8.3	1.6

Appendix B

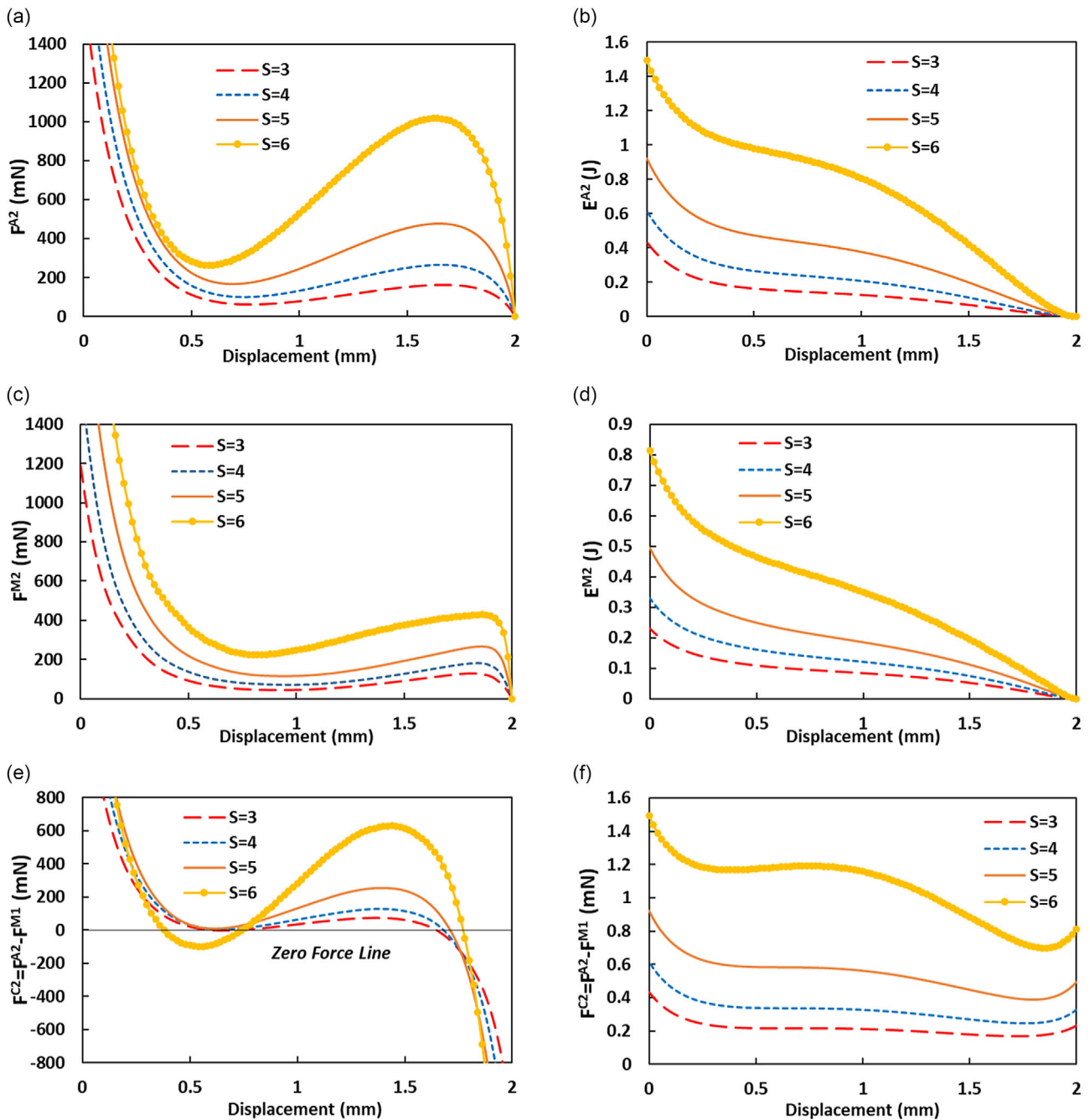


Figure B1. a,b) Force and energy versus displacement of a single SMA beam in austenite state with memory shape at maximum displacement $\Delta z_{\max} = 2$ mm. c,d) Force and energy versus displacement of a single SMA beam in martensite state. e,f) Coupling force F^{C2} and energy E^{C2} versus displacement for case 2, whereby SMA beam 2 is in austenitic and fully deflected state at $z = 0$, while SMA beam 1 is martensitic and in undeflected state [$F^{C2}(z) = F^{A2}(\Delta z_{\max} - z) - F^{M1}(z)$, $E^{C2}(z) = E^{A2}(\Delta z_{\max} - z) + E^{M1}(z)$]. The memory shape of SMA beam 2 is at maximum displacement $\Delta z_{\max} = 2$ mm. In each case, the spacer length S is varied as indicated, while the initial out-of-plane deflection h is kept at $h = 1$ mm and the bending radius of the SMA beam end is in the tangential limit $R = R_{\text{tan}}$.

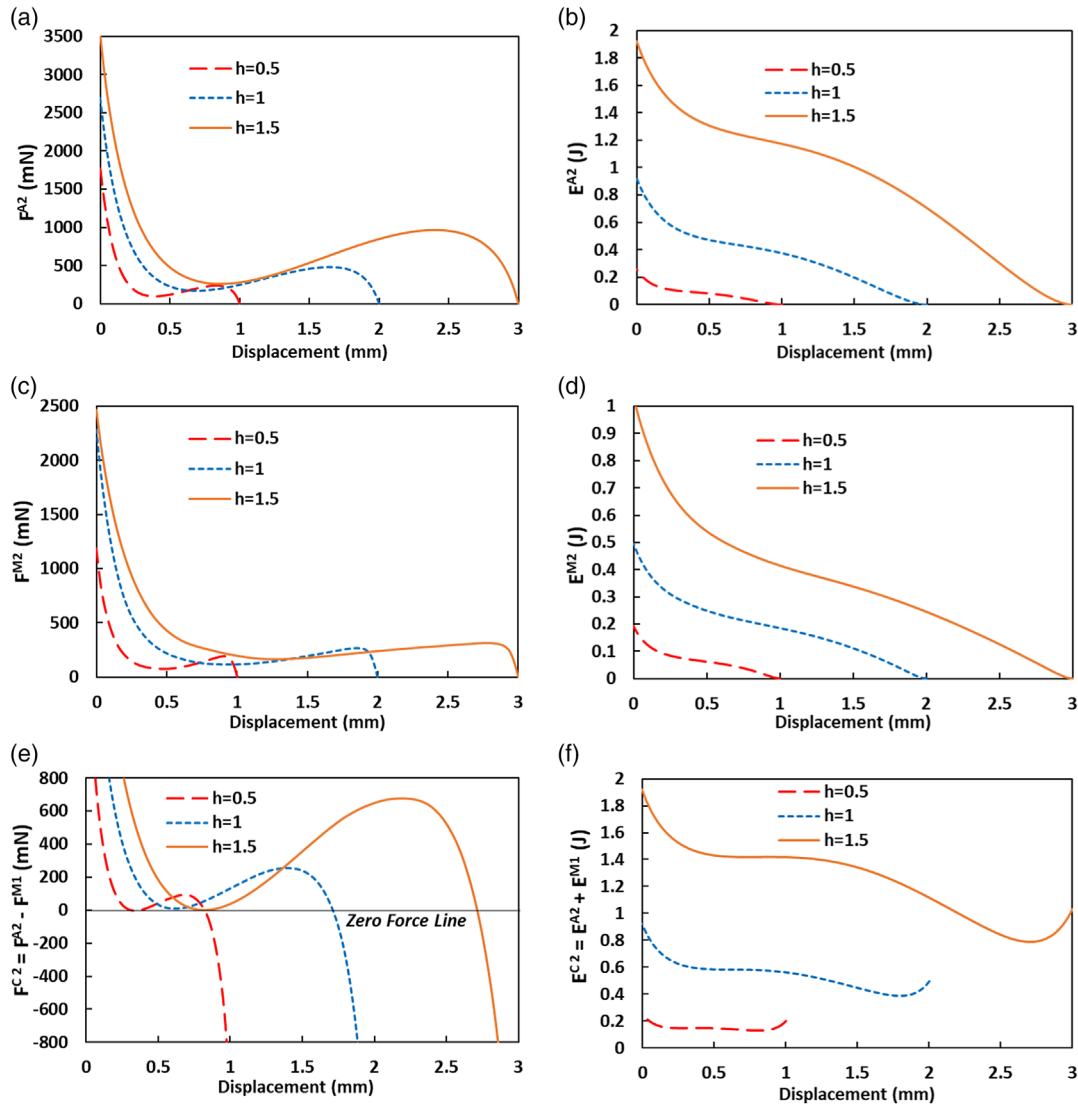


Figure B2. a,b) Force and energy versus displacement of a single SMA beam in austenite state with memory shape at maximum displacement $\Delta z_{\max} = 2$ mm. c,d) Force and energy versus displacement of a single SMA beam in martensite state. e,f) Coupling force F^{C2} and energy E^{C2} versus displacement for case 2, whereby SMA beam 2 is in austenitic and fully deflected state at $z = 0$, while SMA beam 1 is martensitic and in undeflected state [$F^{C2}(z) = F^{A2}(\Delta z_{\max} - z) - F^{M1}(z)$, $E^{C2}(z) = E^{A2}(\Delta z_{\max} - z) + E^{M1}(z)$]. The memory shape of SMA beam 2 is at maximum displacement $\Delta z_{\max} = 2$ mm. In each case, the initial out-of-plane deflection h is varied as indicated, while the spacer length S is kept at $S = 5$ mm and the bending radius of the SMA beam end is in the tangential limit $R = R_{\tan}$.

Appendix C

Considering the geometrical equation in Z direction from Figure 2, we have

$$2(R_{\tan} \sin(\theta) + r \sin(\theta)) + S = L \quad (C1)$$

$$(R_{\tan} + r)(2 \sin(\theta)) + S = L \quad (C2)$$

$$(R_{\tan} + r) = \frac{L - S}{2 \sin(\theta)} \quad (C3)$$

Also, based on a geometrical equation in Y direction, we have

$$R_{\tan}(1 - \cos(\theta)) + r(1 - \cos(\theta)) = h \quad (C4)$$

$$(R_{\tan} + r)(1 - \cos(\theta)) = h \quad (C5)$$

$$(R_{\tan} + r) = \frac{h}{1 - \cos(\theta)} \quad (C6)$$

Using two Equation (C3) and (C6)

$$1 - \cos(\theta) = \frac{2h}{L-S} \sin(\theta) \quad (C7)$$

Suppose α as below

$$\alpha = \frac{2h}{L-S} \quad (C8)$$

Considering Pythagorean identity and substituting Equation (C8) in C7, a quadratic equation is obtained (Equation (C9)) for $\cos(\theta)$ wherein its solution (Equation (C10)) and available $\cos(\theta)$ are derived in Equation (C11).

$$(1 + \alpha^2)\cos^2(\theta) - 2\cos(\theta) + (1 - \alpha^2) = 0 \quad (C9)$$

$$\cos(\theta) = \frac{2 \pm \sqrt{4 - 4(1 + \alpha^2)(1 - \alpha^2)}}{2(1 + \alpha^2)} = \frac{2 \pm \sqrt{4\alpha^4}}{2(1 + \alpha^2)} = \frac{1 \pm \alpha^2}{1 + \alpha^2} \quad (C10)$$

$$\text{Sol.1: } \cos(\theta) = \frac{1 + \alpha^2}{1 + \alpha^2} = 1 \quad \times \quad (\text{Impossible Solution}) \quad (C11)$$

$$\text{Sol.2: } \cos(\theta) = \frac{1 - \alpha^2}{1 + \alpha^2} \quad \checkmark \quad (\text{Possible Solution})$$

In the following, by substituting available value for $\cos(\theta)$ from Equation (C11) in Equation (C5) and then using Equation (C8), we have

$$\begin{aligned} h &= (R_{\tan} + r)(1 - \cos(\theta)) = (R_{\tan} + r) \left(1 - \frac{1 - \alpha^2}{1 + \alpha^2}\right) \\ &= (R_{\tan} + r) \left(\frac{2\alpha^2}{1 + \alpha^2}\right) \\ &= (R_{\tan} + r) \left(\frac{2\left(\frac{2h}{L-S}\right)^2}{1 + \left(\frac{2h}{L-S}\right)^2}\right) = (R_{\tan} + r) \left(\frac{\frac{8h^2}{(L-S)^2}}{\frac{(L-S)^2 + 4h^2}{(L-S)^2}}\right) \\ &= (R_{\tan} + r) \left(\frac{8h^2}{(L-S)^2 + 4h^2}\right) \end{aligned} \quad (C12)$$

By a mathematical manipulation, another quadratic equation is obtained for “ h ” (Equation (C13)), where its solution (Equation (C14)) and available “ h ” are derived in Equation (C15) as follows.

$$4h^2 - 8(R_{\tan} + r)h + (L - S)^2 = 0 \quad (C13)$$

$$\begin{aligned} h &= \frac{8(R_{\tan} + r) \pm \sqrt{64(R_{\tan} + r)^2 - 16(L - S)^2}}{8} \\ &= (R_{\tan} + r) \pm \sqrt{(R_{\tan} + r)^2 - \left(\frac{L - S}{2}\right)^2} \end{aligned} \quad (C14)$$

$$\begin{aligned} \text{Sol.1: } h &= (R_{\tan} + r) + \sqrt{(R_{\tan} + r)^2 - \left(\frac{L - S}{2}\right)^2} \\ &\quad \times \quad (\text{Impossible Solution}) \end{aligned} \quad (C15)$$

$$\begin{aligned} \text{Sol.2: } h &= (R_{\tan} + r) - \sqrt{(R_{\tan} + r)^2 - \left(\frac{L - S}{2}\right)^2} \\ &\quad \checkmark \quad (\text{Possible Solution}) \end{aligned}$$

Appendix D

Table D1. Details of FE Modeling and Analysis.

No.	Detail	Value/Description
1	Used software	ABAQUS + FORTRAN
2	FE discretization method	An implicit discretization method is used for the constitutive model (UMAT)
3	SMA beam longitudinal mesh size	0.05 mm in L direction (see Figure 2)
4	SMA beam horizontal mesh size	0.05 mm in W direction (see Figure 2)
5	SMA beam thickness mesh size	0.01 mm in t direction (see Figure 2)
6	Damping factor	0.002: damping factor for automatic stabilization
7	Element type	C3D20RT: 20-node triquadratic displacement, trilinear temperature, reduced integration–hexagonal sweep mapped
8	Time steps	1 s
9	SMA material properties	As per Table 1
10	Spacer material properties	$E = 2.9 \text{ GPa}$, $\nu = 0.49$, $\rho = 1190 \text{ Kg m}^{-3}$
11	Spacer mesh size	0.05 mm in all directions
12	Boundary conditions (BCs)	Mixing of translational and fixed BC in four steps as presented in Section 5.1
13	Contact	Tie constraint between SMA beams and spacer
14	Increment size	Automatic: initial = 1e-6, minimum = 1e-30, maximum = 0.01

Acknowledgements

This work has been funded within the framework of the German Priority Program SPP2206 KOMMMA on Cooperative Multistage Multistable Microactuator Systems.

Open Access funding enabled and organized by Projekt DEAL.

Conflict of Interest

The authors declare no conflict of interest.

Author Contributions

Hamid Shahsavari: Conceptualization (lead); Data curation (lead); Formal analysis (lead); Investigation (lead); Methodology (equal); Project administration (equal); Resources (equal); Software (lead); Validation (equal); Visualization (lead); Writing-original draft (lead); Writing-review and editing (lead). **Xi Chen:** Data curation (supporting); Investigation (supporting). **Georgino Kaleng Tshikwand:** Data curation (supporting); Formal analysis (supporting); Software (supporting); Visualization (supporting). **Frank Wendler:** Conceptualization (supporting); Data curation (supporting); Formal analysis (supporting); Software (supporting); Writing-review and editing (supporting). **Manfred Kohl:** Conceptualization (lead); Formal analysis (supporting); Funding acquisition (lead); Investigation (equal); Methodology (lead); Project administration (lead); Resources (lead); Supervision (lead); Writing-original draft (lead); Writing-review and editing (lead).

Data Availability Statement

The data that support the findings of this study are available from the corresponding author upon reasonable request.

Keywords

active bistability, antagonistic actuation, beam actuators, shape memory alloys

Received: April 22, 2024
Revised: September 4, 2024
Published online:

[1] K. Otsuka, C. M. Wayman, *Shape Memory Materials* Cambridge university press, Cambridge, UK **1999**.
[2] O. Heczko, H. Seiner, S. Fähler, *MRS Bull.* **2022**, 47, 618.
[3] I. Ohkata, Y. Suzuki, *Shape Memory Mater.* **1998**, 240-266.
[4] K. Hu, K. Rabenorosoa, M. Ouisse, *Front. Robot. AI*, **2021**, 8, 678486.
[5] G. Costanza, M. E. Tata, *Materials* **2020**, 13, 1856.
[6] S. Zaidi, F. Lamarque, C. Prella, O. Carton, A. Zeinert, *Smart Mater. Struct.* **2012**, 21, 115027.
[7] S. K. Patel, B. Behera, B. Swain, R. Roshan, D. Sahoo, A. Behera, *Mater. Today: Proc.* **2020**, 33, 5548.
[8] M. Kohl, *Shape Memory Microactuators*, Springer Science & Business Media, Berlin, Germany **2004**.
[9] S. Miyazaki, Y. Q. Fu, W. M. Huang, *Thin Film Shape Memory Alloys: Fundamentals and Device Applications*, Cambridge University Press, New York, NY **2009**.
[10] M. Kohl, R. Fechner, M. Gueltig, C. Megnin, H. Ossmer, in *ACTUATOR 2018; 16th Int Conf. New Actuators*, VDE, Bremen, Germany **2018**.

[11] J. J. Gill, D. T. Chang, L. A. Momoda, G. P. Carman, *Sens. Actuators, A* **2001**, 93, 148.
[12] T. Grund, R. Guerre, M. Despont, M. Kohl, *Eur. Phys. J. Spec. Top.* **2008**, 158, 237.
[13] S. Braun, N. Sandstrom, G. Stemme, W. van der Wijngaart, *J. Microelectromech. Syst.* **2009**, 18, 1309.
[14] T. Grund, C. Megnin, J. Barth, M. Kohl, *J. Microelectron. Electron. Packag.* **2009**, 6, 219.
[15] I. Stachiv, E. Alarcon, M. Lamac, *Metals* **2021**, 11, 415.
[16] M. Kohl, H. Ossmer, M. Gueltig, C. Megnin, *Shape Memory Superelasticity* **2018**, 4, 127.
[17] C. Megnin, B. Moradi, J. Zuern, H. Ossmer, M. Gueltig, M. Kohl, *Microsyst. Technol.* **2020**, 26, 793.
[18] M. S. Kim, J. K. Heo, H. Rodrigue, H. T. Lee, S. Pané, M. W. Han, S. H. Ahn *Adv. Mater.* **2023**, 35, 2208517.
[19] H. Hussein, M. I. Younis, *J. Mech. Rob.* **2020**, 12, 041001.
[20] V. Deshpande, O. Myers, G. Fadel, S. Li, *Compos. Sci. Technol.* **2021**, 211, 08871.
[21] D. Niu, D. Li, M. Xiong, J. Chen, Y. Cao, J. Chen, H. Liu, *Adv. Eng. Mater.* **2023**, 25, 2201268.
[22] A. Micheletti, *Smart Mater. Struct.* **2018**, 27, 105028.
[23] F. Amarante dos Santos, C. Bedon, A. Micheletti. *Struct. Control Health Monit.* **2020**, 27, e2463.
[24] Y. Chi, Y. Li, Y. Zhao, Y. Hong, Y. Tang, J. Yin, *Adv. Mater.* **2022**, 34, 2110384.
[25] J. Joseph, M. Ohtsuka, H. Miki, M. Kohl, *Actuators* **2023**, 12, 245.
[26] G. K. Tshikwand, L. Seigner, F. Wendler, M. Kohl, *Shape Memory Superelasticity* **2022**, 8, 373.
[27] M. B. Shamim, M. Hörsting, S. Wulfinghoff. *Actuators* **2023**, 12, 36.
[28] Y. Cao, M. Derakhshani, Y. Fang, G. Huang, C. Cao, *Adv. Funct. Mater.* **2021**, 31, 2106231.
[29] S. M. Curtis, M. Sielenkämper, G. Arivanandhan, D. Dengiz, Z. Li, J. Jetter, L. Hanke, L. Bumke, E. Quandt, S. Wulfinghoff, M. Kohl, *Int. J. Smart Nano Mater.* **2022**, 13, 293.
[30] J. Barth, B. Krevet, M. Kohl, *Smart Mater. and Struct.* **2010**, 19, 094004.
[31] M. Gueltig, F. Wendler, H. Ossmer, M. Ohtsuka, H. Miki, T. Takagi, M. Kohl, *Adv. Energy Mater.* **2017**, 7, 1601879.
[32] R. Gao, M. Li, Q. Wang, J. Zhao, S. Liu, *Sens. Actuators A* **2018**, 272, 295.
[33] J. Zhang, Z. Wu, C. Zhang, L. Hao, R. Nie, J. Qiu, *Smart Mater. Struct.* **2019**, 28, 055009.
[34] A. Amor, A. Fernandes, J. Pouget, *Int. J. Non-Linear Mech.* **2020**, 119, 103358.
[35] M. Derakhshani, N. Momenzadeh, T. A. Berfield, *J. Sound Vib.* **2021**, 497, 115937.
[36] B. Camescasse, A. Fernandes, J. Pouget, *Int. J. Solids Struct.* **2014**, 51, 1750.
[37] J. Hua, H. Lei, C.-F. Gao, X. Guo, D. Fang, *Extreme Mech. Lett.* **2020**, 35, 100640.
[38] L. Brinson, R. Lammering, *Int. J. Solids Struct.* **1993**, 30, 3261.
[39] D. C. Lagoudas, P. B. Entchev, P. Popov, E. Patoor, L. C. Brinson, X. Gao, *Mech. Mater.* **2006**, 38, 430.
[40] J. Arghavani, F. Auricchio, R. Naghdabadi, *Int. J. Plast.* **2011**, 27, 940.
[41] P. Sedlak, M. Frost, B. Benešová, T. B. Zineb, P. Šittner, *Int. J. Plast.* **2012**, 39, 132.
[42] M. Sielenkämper, S. Wulfinghoff, *Acta Mech* **2022**, 233, 3059.
[43] M. E. Gurtin, E. Fried, L. Anand, *The Mechanics and Thermodynamics of Continua*, Cambridge university press, New York, USA **2010**.
[44] B. D. Coleman, W. Noll, *Arch. Ration. Mech. Anal.* **1963**, 13, 167.
[45] X. Chen, L. Bumke, E. Quandt, M. Kohl, *Actuators* **2023**, 12, 422.